

Electrically controlling single-spin qubits in a continuous microwave field

Arne Laucht,^{1*} Juha T. Muhonen,¹ Fahd A. Mohiyaddin,¹ Rachpon Kalra,¹ Juan P. Dehollain,¹ Solomon Freer,¹ Fay E. Hudson,¹ Menno Veldhorst,¹ Rajib Rahman,² Gerhard Klimeck,² Kohei M. Itoh,³ David N. Jamieson,⁴ Jeffrey C. McCallum,⁴ Andrew S. Dzurak,¹ Andrea Morello^{1*}

Large-scale quantum computers must be built upon quantum bits that are both highly coherent and locally controllable. We demonstrate the quantum control of the electron and the nuclear spin of a single ^{31}P atom in silicon, using a continuous microwave magnetic field together with nanoscale electrostatic gates. The qubits are tuned into resonance with the microwave field by a local change in electric field, which induces a Stark shift of the qubit energies. This method, known as A-gate control, preserves the excellent coherence times and gate fidelities of isolated spins, and can be extended to arbitrarily many qubits without requiring multiple microwave sources.

The construction of a large-scale quantum computer is among the most exciting scientific challenges of our time. For this purpose, the ability to exploit the advanced fabrication methods developed in semiconductor nanoelectronics (1, 2) would be highly beneficial. Succeeding at this project will depend on the ability to create quantum bits (qubits), which are, at the same time, highly coherent and easy to control and couple to each other. However, quantum coherence and ease of control are often antithetic requirements. Several types of semiconductor spin qubits have been designed to be operated using only electric fields (3–6). This allows control at the nanometer scale via small electrodes but can lead to unwanted decoherence from charge and gate noise (7, 8). Other spin qubits, such as the electrons and nuclei of ^{31}P donors in silicon (9, 10) or nitrogen-vacancy centers in diamond (11, 12), exhibit outstanding coherence times thanks to their lack of sensitivity to electrical noise and the reduced nuclear spin fluctuations in their vicinity. However, their coherent operation requires high-frequency oscillating magnetic fields, which are difficult to confine to nanometer scales. A solution to reconcile long coherence with local electrical control was already described in the visionary proposal of Kane (13) for a donor-based quantum computer in silicon. The resonance frequency of a ^{31}P donor spin depends on the applied magnetic field B_0 , as well as the electron-nuclear hyperfine coupling A . The latter can be locally tuned with an electrostatic gate, known as the “A-gate,” which deforms the wavefunction of the donor-bound electron and modifies the probability density at the nucleus (14). Kane envisaged a multi-qubit quantum computer where a global, always-on microwave magnetic field is by default off-resonance with the qubits. Quantum operations are controlled by locally modifying A to bring the desired qubits into resonance with the global microwave field (15). This eminently scalable proposal has been further developed to include quantum error correction (16). Here, we present the experimental demonstration of local and coherent electrical control of both the electron and

the nuclear spin of a single ^{31}P donor in silicon, representing the first realization of Kane’s A-gate on a single qubit.

The ^{31}P donor in silicon constitutes a two-qubit system, where both the electron (indicated with $|\downarrow\rangle$ or $|\uparrow\rangle$) and the nuclear ($|\psi\rangle$ or $|\uparrow\rangle$) spin states can be coherently controlled by a magnetic field B_1 oscillating at specific electron spin resonance (ESR) and nuclear magnetic resonance (NMR) frequencies. We fabricated a device that comprises a single ^{31}P donor in an isotopically purified ^{28}Si epilayer (17), implanted (18) next to the island of a single-electron transistor (SET). The SET is formed under an 8-nm-thick SiO_2 layer by biasing a set of electrostatic gates (yellow in Fig. 1A). The distance between the donor and SET island is $\sim 20(5)$ nm, resulting in a tunnel coupling of order 10 kHz. The device is cooled by a dilution refrigerator (electron temperature $T_{\text{el}} \approx 100$ mK) and subjected to a static magnetic field $B_0 = 1.55$ T applied along the [110] Si crystal axis. Because of the Zeeman effect, the electrochemical potential μ of the donor electron depends on its spin state, with $\mu_{\uparrow} > \mu_{\downarrow}$. Another set of gates (pink in Fig. 1A) is used to tune the electrochemical potentials of donor and SET island (μ_{SET}) to the readout position (“Read/Init.” in Fig. 2A), where $\mu_{\uparrow} > \mu_{\text{SET}} > \mu_{\downarrow}$ and only the $|\uparrow\rangle$ state can tunnel out of the donor. The positive donor charge left behind shifts the SET bias point and causes a current to flow, until a $|\downarrow\rangle$ electron tunnels back onto the donor. This spin-dependent tunneling mechanism is therefore used to achieve single-shot electron spin readout (19, 20), as well as $|\downarrow\rangle$ initialization. For coherent spin control, an oscillating magnetic field B_1 is delivered to the donor by an on-chip, broadband transmission line terminating in a short-circuited nanoscale antenna (21) (blue in Fig. 1A). While manipulating the electron spin state, the gates are tuned such that $\mu_{\uparrow, \downarrow} < \mu_{\text{SET}}$ to ensure that the electron cannot escape the donor (“Pulse ESR/NMR” and “A-Gate Control” positions in Fig. 2A).

In the present experiment, the same gates used to tune the donor to the readout position are also used to apply an electric field shift, which in turn modifies the spin transition frequencies via the Stark effect. Therefore, we label them A-gates henceforth. In Fig. 1B, we illustrate the effect of the electric field on the donor electron. A positive bias on a gate located above the donor pulls the electron wavefunction toward the Si/SiO₂ interface and away from the nucleus (14). This modifies both the hyperfine coupling A (≈ 117.53 MHz in bulk, and 96.9 MHz for this device) (14, 22) and the electron gyromagnetic ratio γ_e (≈ 27.97 GHz/T in bulk) (23). The ESR frequencies $\nu_{\text{e}1,2}$ depend on both these parameters and on the state of the ^{31}P nuclear spin.

¹Centre for Quantum Computation and Communication Technology, School of Electrical Engineering and Telecommunications, University of New South Wales, Sydney, New South Wales 2052, Australia. ²Network for Computational Nanotechnology, Purdue University, West Lafayette, IN 47907, USA. ³School of Fundamental Science and Technology, Keio University, 3-14-1 Hiyoshi, Kohoku-ku, Yokohama 223-8522, Japan. ⁴Centre for Quantum Computation and Communication Technology, School of Physics, University of Melbourne, Melbourne, Victoria 3010, Australia.

*Corresponding author. E-mail: a.laucht@unsw.edu.au (A.L.); a.morello@unsw.edu.au (A.M.)

Fig. 1. Electric field dependence of electron and nuclear energy states. (A) False-colored scanning electron microscope image of a device similar to the one used in the experiment. Blue, microwave (MW) antenna; yellow, gates used to induce the SET charge sensor under the SiO₂ insulator; pink, A-gates, comprising gates labeled Donor Fast (DF), Donor Slow (DS), and Top Gate AC (TGAC). These gates are used to tune the potential and electric field at the donor location. (B) Electron wavefunction of a donor under an electrostatic gate. A positive voltage applied to the gate attracts the electron toward the Si-SiO₂ interface. For illustration purposes, the wavefunction distortion is largely exaggerated as compared to the actual effect taking place in the experiment. (C) Energy level diagram of the neutral e⁻³¹P system. Gate-controlled distortion of the electron wavefunction modifies A and γ_e , shifting the ESR ν_{e1} and ν_{e2} , and the NMR ν_{n1} and ν_{n2} transition frequencies.

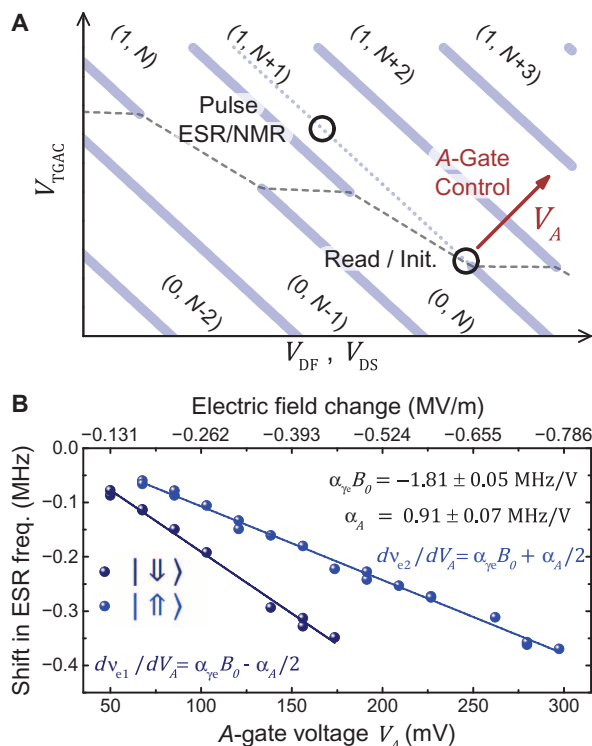
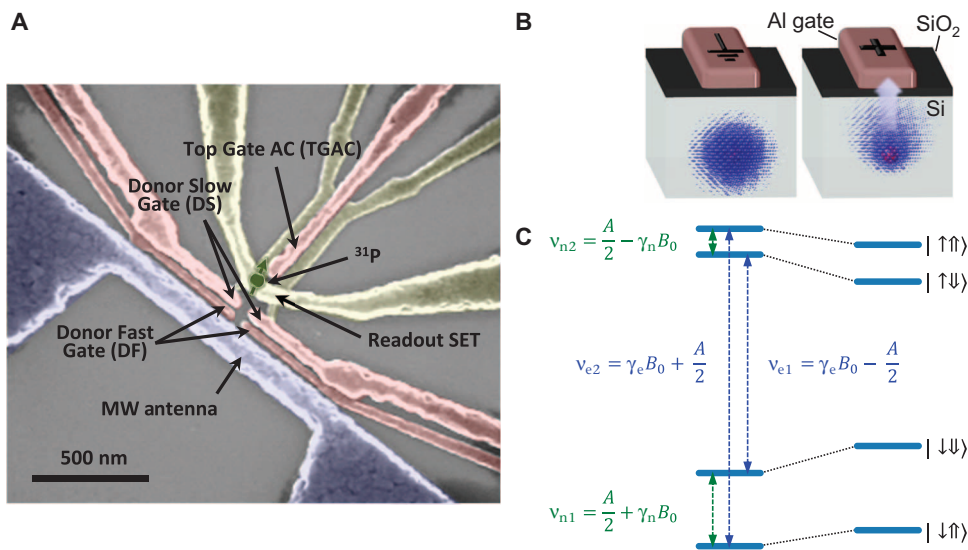


Fig. 2. Local electrical control of the ESR transition frequencies. (A) Schematic of the charge stability diagram for this device. The thick solid lines represent the Coulomb peaks of the SET, whereas the dashed line indicates the ionization/neutralization of the donor. (B) Measured shift in ESR frequencies $\nu_{e1,2}(V_A)$ as a function of the A-gate voltage V_A . Accurate values of $\nu_{e1,2}(V_A)$ are obtained by coherent Ramsey experiments (see text). The change in local electric field is obtained from finite element electrostatic modeling for the specific device geometry and donor location (see section S6 for details).

In the limit $\gamma_e B_0 \gg A$, we find $\nu_{e1} = \gamma_e B_0 - A/2$ (for nuclear spin $|\downarrow\rangle$) and $\nu_{e2} = \gamma_e B_0 + A/2$ (for $|\uparrow\rangle$), as shown in Fig. 1C. Identifying whether the instantaneous ESR frequency is ν_{e1} or ν_{e2} constitutes a

single-shot, quantum nondemolition nuclear spin readout (10). The NMR transitions can be gate-tuned as well, albeit only via the Stark shift of A , because $\nu_{n1} = A/2 + \gamma_n B_0$ (for electron spin $|\downarrow\rangle$) and $\nu_{n2} = A/2 - \gamma_n B_0$ (for $|\uparrow\rangle$), where $\gamma_n = 17.23$ MHz/T is the ³¹P nuclear gyromagnetic ratio.

During pulse ESR/NMR experiments, we normally operate the electrostatic gates in a compensated manner to keep μ_{SET} constant while shifting $\mu_{\uparrow,\downarrow}$ with respect to it (19) (“Pulse ESR/NMR” position in Fig. 2A). This, however, results in a limited variation of the electric field at the donor site. To induce a significant Stark shift, we adopted an uncompensated gating scheme, where both $\mu_{\uparrow,\downarrow}$ and μ_{SET} are drastically lowered (“A-Gate Control” position in Fig. 2A; see section S4 for details on the exact gate configuration). The resulting change in electric field can be calculated with a finite element Poisson equation solver (TCAD) for the specific device geometry and the triangulated donor location (see sections S5 and S6 for details) (24).

We demonstrate the gate-induced shift of the ESR frequencies by performing, with conventional pulse ESR, a series of Ramsey experiments on the electron spin at different values of V_A (Fig. 2B), where we define $V_A = 0$ as the readout position. The spin is rotated from $|\downarrow\rangle$ to the xy plane by a $\pi/2$ pulse at frequency ν_{MW} , left to freely precess for a time τ , and then rotated by $\pi/2$ again. The accumulation of a phase shift between the spin precession at $\nu_e(V_A)$ and the MW reference clock at ν_{MW} gives rise to oscillations in the probability of finding the electron $|\uparrow\rangle$ at the end of the sequence. The frequency of the Ramsey fringes gives a very accurate value for $\nu_e(V_A) - \nu_{\text{MW}}$.

Both ν_{e1} and ν_{e2} shift to lower frequencies upon increasing V_A (Fig. 2B). This indicates that a significant Stark shift of γ_e (that is, the electron g -factor) is taking place, in addition to the A -shift. Linear fits to $\nu_{e1,2}(V_A)$ yield slopes $d\nu_{e1}/dV_A = -2.27(6)$ MHz/V and $d\nu_{e2}/dV_A = -1.36(3)$ MHz/V. Using the expressions given in Fig. 2B, we extract the tuning parameters $\alpha_A = dA/dV_A = d\nu_{e2}/dV_A - d\nu_{e1}/dV_A = 0.91(7)$ MHz/V and $\alpha_{\gamma_e B_0} = d\gamma_e B_0/dV_A = (d\nu_{e2}/dV_A + d\nu_{e1}/dV_A)/2 = -1.81(5)$ MHz/V, with $\alpha_{\gamma_e} = d\gamma_e/dV_A = -1.17(3)$ MHz/V/T at $B_0 = 1.55$ T. The positive value of α_A indicates that increasing V_A leads to an increase in the electron probability density at the nucleus. This is because a strong electric field is already present for the purpose of forming the SET, whereas increasing V_A causes an additional electric field in the opposite

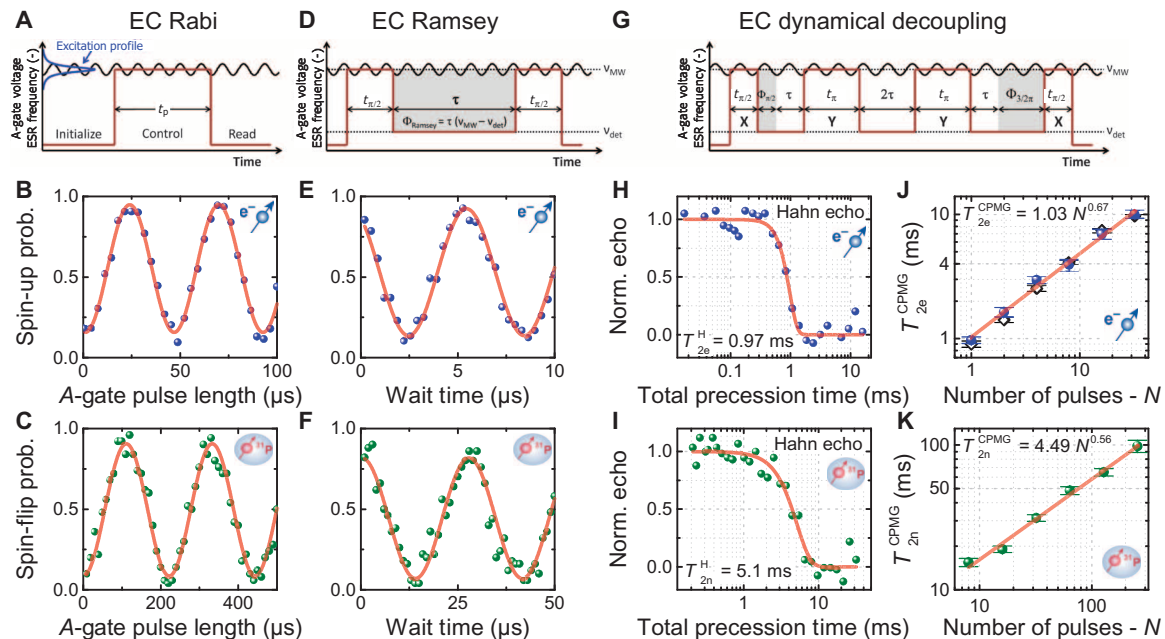


Fig. 3. Electrically controlled qubit control and coherence measurements. (A) Schematic of the sequence used to measure EC Rabi oscillations. (B and C) EC Rabi oscillations measured on the ^{31}P electron and nucleus, respectively. (D) Schematic of the sequence used to measure EC Ramsey oscillations. (E and F) EC Ramsey oscillations

direction, thus an overall reduction of the hyperfine Stark shift (see finite element simulations in section S6). The absolute value of the hyperfine coupling and its tunability is in agreement with atomistic tight-binding simulations with NEMO-3D (25, 26) for the range of donor positions, electric fields, and strain expected for this device (see section S7).

An A-gate voltage $V_A \sim 300$ meV results in a frequency tuning range $\Delta V_e^{\text{max}} = 400$ to 700 kHz. Thanks to the use of an isotopically enriched ^{28}Si epilayer (17), this is a factor >200 larger than the intrinsic linewidth $\delta\nu_e^{\text{FWHM}} = 1.8$ kHz of the ESR transitions (22). For the same V_A , the NMR frequencies can be shifted by $\Delta\nu_n^{\text{max}} = 125$ to 150 kHz by the Stark shift of A alone, which is a factor ~ 250 higher than the intrinsic linewidth $\delta\nu_n^{\text{FWHM}} = 0.5$ kHz (22).

Having calibrated the voltage-controlled qubit frequency shifts, we demonstrate how to use A-gate pulses to perform coherent control of the qubit states around the Bloch sphere in the presence of a continuous-wave (CW) oscillating magnetic field B_1 . We demonstrate this on both the electron and the nuclear spin qubits. Figure 3A is a schematic of the electrically controlled Rabi sequence. We pulse V_A to V_r , the voltage needed to tune the spin transition in resonance with the MW or RF source, for a time t_p , to coherently drive the spin around the x axis of the Bloch sphere, defined in the reference frame rotating at ν_{MW} (for ESR) or ν_{RF} (for NMR). The coherent Rabi oscillations (Fig. 3, B and C) are used to calibrate the duration of the control pulses for any desired rotation angle.

An electrically controlled Ramsey experiment (Fig. 3D) is obtained by tuning the spin transition frequencies into resonance for the duration of a $\pi/2$ rotation, then moving them to a detuned value ν_{det} for a wait time τ to accumulate a phase shift $\Phi_R = \tau(\nu(V_r) - \nu_{\text{det}})$ with respect to the $\nu(V_r)$ reference frame, and finally tuning them back into resonance for the second $\pi/2$ rotation (Fig. 3, E and F). Qubit rotations

measured on the ^{31}P electron and nucleus. (G) Schematic of the sequence used to measure EC coherence times. (H and I) EC Hahn echo decay for the ^{31}P electron and nucleus. (J and K) Extended spin coherence times T_2 for CPMG dynamical decoupling sequences on the ^{31}P electron and nucleus.

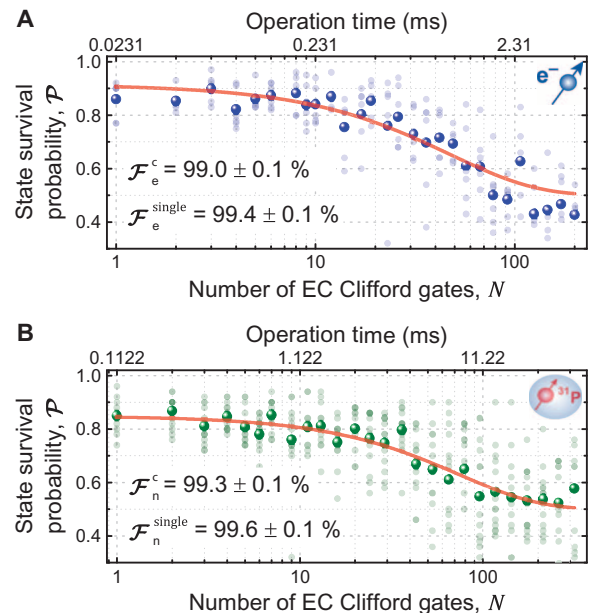


Fig. 4. Electrically controlled gate fidelities. (A and B) EC randomized benchmarking performed on the ^{31}P electron and nucleus, respectively. Shaded circles are the results of individual measurements (that is, individual random sequences of gate operations), whereas the solid circles show the average state survival probability of all random sequences with the same number of gate operations.

around the y axis can be achieved by accumulating an additional $\Phi_R = \pi/2$ before bringing the spin into resonance. This allows for full two-axis (x and y) control of the qubits' states on the Bloch sphere.

Alternatively, we can produce a Z-gate by controlling the phase Φ_R that the qubit accumulates while off-resonance.

We measure the qubits' coherence times T_2 by performing Hahn echo and Carr-Purcell-Meiboom-Gill (CPMG) dynamical decoupling sequences (Fig. 3, G to K). For these measurements, the wait times τ are chosen such that they always result in a multiple of 2π phase shift. The Hahn echo yields $T_{2e}^H = 0.97(6)$ ms and $T_{2n}^H = 5.1(3)$ ms for the donor electron and nuclear spins, respectively (Fig. 3, H and I). A CPMG sequence (see schematic in Fig. 3G for details) further decouples the qubits from low-frequency noise and extends the coherence times to up to $T_{2e}^{\text{CPMG}} = 10.0(8)$ ms and $T_{2n}^{\text{CPMG}} = 98(9)$ ms by applying 32 and 256 π pulses, respectively (Fig. 3, J and K). The coherence times of the electrically controlled electron qubit, measured in milliseconds, can be fitted by $T_{2e}^{\text{CPMG}}(N) = 1.03N^{0.67}$. Conventional pulse ESR operation (black diamonds in Fig. 3J) gives nearly identical values, $T_{2e}^{\text{pulseCPMG}} = 0.93N^{0.70}$ (see also section S10 for more data). The electrical control method preserves the excellent spin coherence of the qubits, because no additional coupling between the spin states and the environment has been introduced.

We apply the two-axis control to construct the complete set of 1-qubit Clifford gates, and conduct randomized benchmarking (27, 28) experiments (Fig. 4, A and B) to quantify the average gate fidelities using electrically controlled qubit manipulation (Fig. 4). The method relies upon the measurement of the probability $\mathcal{P}(N)$ of arriving at the correct final qubit state after performing a long sequence of randomly chosen quantum gates. In the presence of gate errors, the probability decays according to the number of operations N . We then extract the average fidelity for a single Clifford gate \mathcal{F}^c by fitting the equation

$$\mathcal{P}(N) = M(2\mathcal{F}^c - 1)^N + 0.5 \quad (1)$$

to the data (28). M is a free parameter and depends on the initialization and readout fidelity. We obtain $\mathcal{F}_e^c = 99.0(1)\%$ and $\mathcal{F}_n^c = 99.3(1)\%$ for the electron and the nuclear spin, respectively. Because each Clifford gate is composed on average of 1.875 individual gate operations (28, 29), we can also quote average single-gate fidelities of $\mathcal{F}_e^{\text{single}} = 99.4(1)\%$ for the electron and $\mathcal{F}_n^{\text{single}} = 99.6(1)\%$ for the nucleus. These gate fidelities are comparable to those obtained by pulse ESR/NMR randomized benchmarking for similar microwave powers (28) and are mostly limited by the ratio of gate time to coherence time.

The speed of an electrically controlled gate operation is inherently limited by the voltage tunability of the resonance frequencies. The excitation profile of the CW field (Fig. 3A) must be narrow enough to leave the qubits unperturbed while off-resonance, imposing the condition $\gamma B_1 \ll \Delta\nu$. For linearly oscillating B_1 , $(\gamma B_1)^{-1}$ is the duration of a π rotation. Therefore, $\Delta\nu < 1$ MHz in this ^{31}P device requires gate times >10 μs .

The qubit control method demonstrated here is applicable to any resonantly driven qubit, where the resonance frequency ν_r can be quickly and locally controlled by an electric field, and shifted by much more than the resonance linewidth. A wide variety of qubits can potentially fulfill this condition. For spins in diamond (30) and silicon carbide (31), ν_r can be tuned by modifying the crystal field parameters in the spin Hamiltonian. Magnetic molecules can have tunable ν_r through a hyperfine Stark effect (32) similar to the one shown here. Several types of semiconductor quantum dot qubits exhibit tunable electron spin g-factor (33, 34) through spin-orbit coupling effects, or

tunable splitting through the interplay of valley-orbit and tunnel couplings (6).

Because of the high cost of vector microwave signal generators, it seems implausible that future multi-qubit experiments will resort to a dedicated source for each qubit. Time- and frequency-multiplexing qubit control is possible in proof-of-principle experiments but is impractical in large fault-tolerant quantum processors. In most error correction schemes, fault tolerance is only guaranteed if all qubits can be operated simultaneously at any time. The method of qubit control demonstrated here fulfills all the practical requirements for a large-scale quantum computer, because control gates can be applied simultaneously to arbitrarily many qubits while requiring only one CW microwave source together with inexpensive multichannel baseband pulse generators.

SUPPLEMENTARY MATERIALS

Supplementary material for this article is available at <http://advances.sciencemag.org/cgi/content/full/1/3/e1500022/DC1>

Fig. S1. Frequency response.

Fig. S2. Donor triangulation.

Fig. S3. Electric field simulations.

Fig. S4. Electric field simulations.

Fig. S5. Electric field simulations.

Fig. S6. Atomistic tight binding simulations of the hyperfine coupling for a donor at the location determined in section S5, for the electric fields simulated in section S6, and subject to lattice strain.

Fig. S7. Electrically controlled ESR spectrum.

Fig. S8. Time evolution simulations of the electrically controlled ESR spectrum.

Fig. S9. Electrically controlled Rabi spectrum.

Fig. S10. Electrically controlled electron Ramsey.

Fig. S11. Electrically controlled nuclear Ramsey.

Fig. S12. Electrically controlled electron coherence times.

Fig. S13. Electrically controlled nuclear coherence times.

Table S1. Relative gate capacitances used for triangulation of the donor position.

References (35–54)

REFERENCES AND NOTES

1. D. D. Awschalom, L. C. Bassett, A. S. Dzurak, E. L. Hu, J. R. Petta, Quantum spintronics: Engineering and manipulating atom-like spins in semiconductors. *Science* **339**, 1174–1179 (2013).
2. F. A. Zwanenburg, A. S. Dzurak, A. Morello, M. Y. Simmons, L. C. L. Hollenberg, G. Klimeck, S. Rogge, S. N. Coppersmith, M. A. Eriksson, Silicon quantum electronics. *Rev. Mod. Phys.* **85**, 961–1019 (2013).
3. J. R. Petta, A. C. Johnson, J. M. Taylor, E. A. Laird, A. Yacoby, M. D. Lukin, C. M. Marcus, M. P. Hanson, A. C. Gossard, Coherent manipulation of coupled electron spins in semiconductor quantum dots. *Science* **309**, 2180–2184 (2005).
4. K. C. Nowack, F. H. L. Koppens, Y. V. Nazarov, L. M. K. Vandersypen, Coherent control of a single electron spin with electric fields. *Science* **318**, 1430–1433 (2007).
5. J. Medford, J. Beil, J. M. Taylor, S. D. Bartlett, A. C. Doherty, E. I. Rashba, D. P. DiVincenzo, H. Lu, A. C. Gossard, C. M. Marcus, Self-consistent measurement and state tomography of an exchange-only spin qubit. *Nat. Nanotechnol.* **8**, 654–659 (2013).
6. D. Kim, Z. Shi, C. B. Simmons, D. R. Ward, J. R. Prance, T. S. Koh, J. K. Gamble, D. E. Savage, M. G. Lagally, M. Friesen, S. N. Coppersmith, M. A. Eriksson, Quantum control and process tomography of a semiconductor quantum dot hybrid qubit. *Nature* **511**, 70–74 (2014).
7. O. E. Dial, M. D. Shulman, S. P. Harvey, H. Bluhm, V. Umansky, A. Yacoby, Charge noise spectroscopy using coherent exchange oscillations in a singlet-triplet qubit. *Phys. Rev. Lett.* **110**, 146804 (2013).
8. E. A. Laird, F. Pei, L. P. Kouwenhoven, A valley-spin qubit in a carbon nanotube. *Nat. Nanotechnol.* **8**, 565–568 (2013).
9. J. J. Pla, K. Y. Tan, J. P. Dehollain, W. H. Lim, J. J. Morton, D. N. Jamieson, A. S. Dzurak, A. Morello, A single-atom electron spin qubit in silicon. *Nature* **489**, 541–545 (2012).
10. J. J. Pla, K. Y. Tan, J. P. Dehollain, W. H. Lim, J. J. Morton, F. A. Zwanenburg, D. N. Jamieson, A. S. Dzurak, A. Morello, High-fidelity readout and control of a nuclear spin qubit in silicon. *Nature* **496**, 334–338 (2013).

11. G. Balasubramanian, I. Y. Chan, R. Kolesov, M. Al-Hmoud, J. Tisler, C. Shin, C. Kim, A. Wojcik, P. R. Hemmer, A. Krueger, T. Hanke, A. Leitenstorfer, R. Bratschkitsch, F. Jelezko, J. Wrachtrup, Nanoscale imaging magnetometry with diamond spins under ambient conditions. *Nature* **455**, 648–651 (2008).
12. P. C. Maurer, G. Kucsko, C. Latta, L. Jiang, N. Y. Yao, S. D. Bennett, F. Pastawski, D. Hunger, N. Chisholm, M. Markham, D. J. Twitchen, J. I. Cirac, M. D. Lukin, Room-temperature quantum bit memory exceeding one second. *Science* **336**, 1283–1286 (2012).
13. B. E. Kane, A silicon-based nuclear spin quantum computer. *Nature* **393**, 133–137 (1998).
14. R. Rahman, C. J. Wellard, F. R. Bradbury, M. Prada, J. H. Cole, G. Klimeck, L. C. Hollenberg, High precision quantum control of single donor spins in silicon. *Phys. Rev. Lett.* **99**, 036403 (2007).
15. G. Wolfowicz, M. Urdampilleta, M. L. Thewalt, H. Riemann, N. V. Abrosimov, P. Becker, H. J. Pohl, J. J. Morton, Conditional control of donor nuclear spins in silicon using stark shifts. *Phys. Rev. Lett.* **113**, 157601 (2014).
16. L. Hollenberg, A. Greentree, A. Fowler, C. Wellard, Two-dimensional architectures for donor-based quantum computing. *Phys. Rev. B* **74**, 045311 (2006).
17. K. M. Itoh, H. Watanabe, Isotope engineering of silicon and diamond for quantum computing and sensing applications. *MRS Commun.* **4**, 143–157 (2014).
18. D. N. Jamieson, C. Yang, T. Hopf, S. M. Hearne, C. I. Pakes, S. Praver, M. Mitic, E. Gauja, S. E. Andresen, F. E. Hudson, A. S. Dzurak, R. G. Clark, Controlled shallow single-ion implantation in silicon using an active substrate for sub-20-keV ions. *Appl. Phys. Lett.* **86**, 202101 (2005).
19. A. Morello, C. C. Escott, H. Huebl, L. H. Willems van Beveren, L. C. L. Hollenberg, D. N. Jamieson, A. S. Dzurak, R. G. Clark, Architecture for high-sensitivity single-shot readout and control of the electron spin of individual donors in silicon. *Phys. Rev. B* **80**, 081307(R) (2009).
20. A. Morello, J. J. Pla, F. A. Zwanenburg, K. W. Chan, K. Y. Tan, H. Huebl, M. Möttönen, C. D. Nugroho, C. Yang, J. A. van Donkelaar, A. D. C. Alves, D. N. Jamieson, C. C. Escott, L. C. L. Hollenberg, R. G. Clark, A. S. Dzurak, Single-shot readout of an electron spin in silicon. *Nature* **467**, 687–691 (2010).
21. J. P. Dehollain, J. J. Pla, E. Siew, K. Y. Tan, A. S. Dzurak, A. Morello, Nanoscale broadband transmission lines for spin qubit control. *Nanotechnology* **24**, 015202 (2013).
22. J. T. Muhonen, J. P. Dehollain, A. Laucht, F. E. Hudson, R. Kalra, T. Sekiguchi, K. M. Itoh, D. N. Jamieson, J. C. McCallum, A. S. Dzurak, A. Morello, Storing quantum information for 30 seconds in a nanoelectronic device. *Nat. Nanotechnol.* **9**, 986–991 (2014).
23. R. Rahman, S. H. Park, T. B. Boykin, G. Klimeck, S. Rogge, L. C. L. Hollenberg, Gate-induced g -factor control and dimensional transition for donors in multivalley semiconductors. *Phys. Rev. B* **80**, 155301 (2009).
24. F. A. Mohiyaddin, R. Rahman, R. Kalra, G. Klimeck, L. C. Hollenberg, J. J. Pla, A. S. Dzurak, A. Morello, Noninvasive spatial metrology of single-atom devices. *Nano Lett.* **13**, 1903–1909 (2013).
25. G. Klimeck, S. S. Ahmed, N. Kharche, M. Korkusinski, M. Usman, M. Prada, T. B. Boykin, Atomistic simulation of realistically sized nanodevices using NEMO 3-D—Part I: Models and benchmarks. *IEEE Trans. Electron Devices* **54**, 2079–2089 (2007).
26. G. Klimeck, S. S. Ahmed, N. Kharche, M. Korkusinski, M. Usman, M. Prada, T. B. Boykin, Atomistic simulation of realistically sized nanodevices using NEMO 3-D—Part II: Applications. *IEEE Trans. Electron Devices* **54**, 2090–2099 (2007).
27. E. Knill, D. Leibfried, R. Reichle, J. Britton, R. B. Blakestad, J. D. Jost, C. Langer, R. Ozeri, S. Seidelin, D. J. Wineland, Randomized benchmarking of quantum gates. *Phys. Rev. A* **77**, 012307 (2008).
28. J. T. Muhonen, A. Laucht, S. Simmons, J. P. Dehollain, R. Kalra, F. E. Hudson, S. Freer, K. M. Itoh, D. N. Jamieson, J. C. McCallum, A. S. Dzurak, A. Morello, Quantifying the quantum gate fidelity of single-atom spin qubits in silicon by randomized benchmarking. *J. Phys. Condens. Matter* **27**, 154205 (2015).
29. J. M. Epstein, A. W. Cross, E. Magesan, J. M. Gambetta, Investigating the limits of randomized benchmarking protocols. *Phys. Rev. A* **89**, 062321 (2014).
30. F. Dolde, H. Fedder, M. W. Doherty, T. Nöbauer, F. Rempp, G. Balasubramanian, T. Wolf, F. Reinhard, L. C. L. Hollenberg, F. Jelezko, J. Wrachtrup, Electric-field sensing using single diamond spins. *Nat. Phys.* **7**, 459–463 (2011).
31. A. L. Falk, P. V. Klimov, B. B. Buckley, V. Ivády, I. A. Abrikosov, G. Calusine, W. F. Koehl, Á. Gali, D. D. Awschalom, Electrically and mechanically tunable electron spins in silicon carbide color centers. *Phys. Rev. Lett.* **112**, 187601 (2014).
32. S. Thiele, F. Balestro, R. Ballou, S. Klyatskaya, M. Ruben, W. Wernsdorfer, Electrically driven nuclear spin resonance in single-molecule magnets. *Science* **344**, 1135–1138 (2014).
33. M. D. Schroer, K. D. Petersson, M. Jung, J. R. Petta, Field tuning the g factor in InAs nanowire double quantum dots. *Phys. Rev. Lett.* **107**, 176811 (2011).
34. M. Veldhorst, J. C. Hwang, C. H. Yang, A. W. Leenstra, B. de Ronde, J. P. Dehollain, J. T. Muhonen, F. E. Hudson, K. M. Itoh, A. Morello, A. S. Dzurak, An addressable quantum dot qubit with fault-tolerant control-fidelity. *Nat. Nanotechnol.* **9**, 981–985 (2014).
35. J. J. Pla, K. Y. Tan, J. P. Dehollain, W. H. Lim, J. J. Morton, D. N. Jamieson, A. S. Dzurak, A. Morello, A single-atom electron spin qubit in silicon. *Nature* **489**, 541–545 (2012).
36. J. J. Pla, K. Y. Tan, J. P. Dehollain, W. H. Lim, J. J. Morton, F. A. Zwanenburg, D. N. Jamieson, A. S. Dzurak, A. Morello, High-fidelity readout and control of a nuclear spin qubit in silicon. *Nature* **496**, 334–338 (2013).
37. F. A. Mohiyaddin, R. Rahman, R. Kalra, G. Klimeck, L. C. Hollenberg, J. J. Pla, A. S. Dzurak, A. Morello, Noninvasive spatial metrology of single-atom devices. *Nano Lett.* **13**, 1903–1909 (2013).
38. Integrated Systems Engineering (ISE), Zurich, *DEVISE, MESH, DESSIS and TECPLOT v10.0 Manual* (2004).
39. K. Nabors, J. White, FastCap: A multipole accelerated 3-D capacitance extraction program. *IEEE Trans. Comput.-Aided Design Integr. Circuits Syst.* **10**, 1447–1459 (1991).
40. B. Johnson, H. U. Rahman, E. Gauja, R. Ramer, J. C. McCallum, Nanoscience and Nanotechnology (ICONN), 2010 International Conference (2010), pp. 333–336.
41. T. Thorbeck, N. M. Zimmerman, Formation of strain-induced quantum dots in gated semiconductor nanostructures. arXiv:1409.3549v1 (2014).
42. C. C. Lo, M. Urdampilleta, P. Ross, M. F. Gonzalez-Zalba, J. Mansir, S. A. Lyon, M. L. W. Thewalt, J. J. L. Morton, Hybrid optical-electrical detection of donor electron spins with bound excitons in silicon. arXiv:1411.1324v1 (2014).
43. A. Morello, J. J. Pla, F. A. Zwanenburg, K. W. Chan, K. Y. Tan, H. Huebl, M. Möttönen, C. D. Nugroho, C. Yang, J. A. van Donkelaar, A. D. Alves, D. N. Jamieson, C. C. Escott, L. C. Hollenberg, R. G. Clark, A. S. Dzurak, Single-shot readout of an electron spin in silicon. *Nature* **467**, 687–691 (2010).
44. E. B. Hale, R. L. Mieher, Shallow donor electrons in silicon. I. Hyperfine Interactions from ENDOR measurements. *Phys. Rev.* **184**, 739 (1969).
45. R. Rahman, S. H. Park, T. B. Boykin, G. Klimeck, S. Rogge, L. C. L. Hollenberg, Gate-induced g -factor control and dimensional transition for donors in multivalley semiconductors. *Phys. Rev. B* **80**, 155301 (2009).
46. A. S. Martins, R. B. Capaz, B. Koiller, Electric-field control and adiabatic evolution of shallow donor impurities in silicon. *Phys. Rev. B* **69**, 085320 (2004).
47. R. Rahman, C. J. Wellard, F. R. Bradbury, M. Prada, J. H. Cole, G. Klimeck, L. C. Hollenberg, High precision quantum control of single donor spins in silicon. *Phys. Rev. Lett.* **99**, 036403 (2007).
48. G. Klimeck, S. S. Ahmed, B. Hansang, N. Kharche, S. Clark, B. Haley, L. Sunhee, M. Naumov, R. Hoon, F. Saied, M. Prada, M. Korkusinski, T. B. Boykin, R. Rahman, Atomistic simulation of realistically sized nanodevices using NEMO 3-D—part I: Models and benchmarks. *Electron Devices, IEEE Transactions* **54**, 2079 (2007).
49. G. Klimeck, S. S. Ahmed, N. Kharche, M. Korkusinski, M. Usman, M. Prada, T. B. Boykin, Atomistic simulation of realistically sized nanodevices using NEMO 3-D—part II: Applications. *Electron Devices, IEEE Transactions* **54**, 2090 (2007).
50. F. A. Mohiyaddin, Designing a large scale quantum computer with classical & quantum simulations, Ph.D. thesis, University of New South Wales (2014).
51. L. Dreher, T. A. Hilker, A. Brandlmaier, S. T. Goennenwein, H. Huebl, M. Stutzmann, M. S. Brandt, Electroelastic hyperfine tuning of phosphorus donors in silicon. *Phys. Rev. Lett.* **106**, 037601 (2011).
52. S. Shevchenko, S. Ashhab, F. Nori, Landau–Zener–Stückelberg interferometry. *Phys. Rep.* **492**, 1–30 (2010).
53. P. Kok, B. W. Lovett, *Introduction to Optical Quantum Information Processing* (Cambridge University Press, 2010).
54. J. T. Muhonen, J. P. Dehollain, A. Laucht, F. E. Hudson, R. Kalra, T. Sekiguchi, K. M. Itoh, D. N. Jamieson, J. C. McCallum, A. S. Dzurak, A. Morello, Storing quantum information for 30 seconds in a nanoelectronic device. *Nat. Nanotechnol.* **9**, 986–991 (2014).

Acknowledgments: We thank S. Simmons, G. Tosi, and C. D. Hill for fruitful discussions and comments. This research was funded by the Australian Research Council Centre of Excellence for Quantum Computation and Communication Technology (project number CE110001027) and the U.S. Army Research Office (W911NF-13-1-0024). We acknowledge support from the Australian National Fabrication Facility and from the laboratory of R. Elliman at the Australian National University for the ion implantation facilities. The work at Keio has been supported in part by FIRST, the Core-to-Core Program by the Japan Society for the Promotion of Science, and the Grant-in-Aid for Scientific Research and Project for Developing Innovation Systems by MEXT. NCN/nanohub.org computational resources funded by the National Science Foundation under contract number EEC-1227110 were used in this work. **Competing interests:** The authors declare that they have no competing interests.

Submitted 8 January 2015

Accepted 14 March 2015

Published 10 April 2015

10.1126/sciadv.1500022

Citation: A. Laucht, J. T. Muhonen, F. A. Mohiyaddin, R. Kalra, J. P. Dehollain, S. Freer, F. E. Hudson, M. Veldhorst, R. Rahman, G. Klimeck, K. M. Itoh, D. N. Jamieson, J. C. McCallum, A. S. Dzurak, A. Morello, Electrically controlling single-spin qubits in a continuous microwave field. *Sci. Adv.* **1**, e1500022 (2015).

This article is published under a Creative Commons license. The specific license under which this article is published is noted on the first page.

For articles published under **CC BY** licenses, you may freely distribute, adapt, or reuse the article, including for commercial purposes, provided you give proper attribution.

For articles published under **CC BY-NC** licenses, you may distribute, adapt, or reuse the article for non-commercial purposes. Commercial use requires prior permission from the American Association for the Advancement of Science (AAAS). You may request permission by clicking [here](#).

The following resources related to this article are available online at <http://advances.sciencemag.org>. (This information is current as of September 24, 2015):

Updated information and services, including high-resolution figures, can be found in the online version of this article at:

<http://advances.sciencemag.org/content/1/3/e1500022.full.html>

Supporting Online Material can be found at:

<http://advances.sciencemag.org/content/suppl/2015/04/07/1.3.e1500022.DC1.html>

This article **cites 47 articles**, 5 of which you can be accessed free:

<http://advances.sciencemag.org/content/1/3/e1500022#BIBL>

Science Advances (ISSN 2375-2548) publishes new articles weekly. The journal is published by the American Association for the Advancement of Science (AAAS), 1200 New York Avenue NW, Washington, DC 20005. Copyright is held by the Authors unless stated otherwise. AAAS is the exclusive licensee. The title *Science Advances* is a registered trademark of AAAS